Progress in Photovoltaics: Research and Applications

WILEY

PROGRESS IN PHOTOVOLTAICS

RESEARCH ARTICLE OPEN ACCESS

Sb_2Se_3 Thin Films for Doping the Absorber in CdTe Solar Cells

Elisa Artegiani[1] | Andrea Gasparotto[2] | Sam Machin[3] | Michael Walls[3] | Alessandro Romeo[1]

[1]LAPS - Laboratory for Photovoltaics and Solid State Physics, Department of Computer Science, University of Verona, Verona, Italy | [2]Department of Physics and Astronomy, University of Padova, Padova, Italy | [3]Centre for Renewable Energy Systems Technology (CREST) Wolfson School of Mechanical, Electrical and Manufacturing Engineering, Loughborough University, Loughborough, UK

Correspondence: Alessandro Romeo (alessandro.romeo@univr.it)

Received: 8 April 2025 | **Revised:** 7 July 2025 | **Accepted:** 11 November 2025

ABSTRACT

Nowadays, the primary efforts in CdTe solar cell research aim to find an alternative to copper doping among the group V elements. In fact, Cu has limited solubility in the CdTe grains, which prevents the achievement of higher open circuit voltages (Voc), and it is also a fast diffuser, considered the main factor of device degradation. Achieving effective doping with an alternative element could lead to improved Voc and, hence, cell efficiency, as well as increased stability. This study presents a novel method to dope CdSeTe/CdTe devices by depositing a thin Sb_2Se_3 layer on top of the absorber. Sb is then driven inside the CdTe matrix by subsequent $CdCl_2$ treatment; the choice of Sb_2Se_3 prevents the introduction of additional impurities. This method proves to be effective because Sb-doped cells achieve efficiencies close to Cu-doped ones. On the other hand, in accelerated stress tests without encapsulation, Sb-containing devices are much more stable than Cu-doped ones, showing the same noteworthy stability as undoped devices.

1 | Introduction

Although research on thin-film photovoltaic technologies is expanding to include more and more materials, cadmium telluride (CdTe) PV modules are still the leading thin-film product in the global market. The efficiency of CdTe devices is improving; over the past 20 years, the record for research-scale cells has risen from 16.5% to 23.1%, recently announced by the US company First Solar. Furthermore, the improvement of the modules' efficiency, now exceeding 19%, together with the increase in production, has led CdTe technology to reach a production cost of just over 0.30$/Wp [1, 2].

To further advance CdTe into commercial applications, it is critical to continue improving its efficiency while keeping production costs low. So far, the increase in efficiency has been mainly due to the introduction of Se into the absorber, with the formation of a CdSeTe alloy near the junction, which significantly improves the current density of the devices and the lifetime of the carriers [3, 4]. Nowadays, efforts should be made to increase the open circuit voltage and stability of devices. Both goals could be achieved by replacing the Cu doping with Group V elements. A higher doping level is needed to improve the voltage, which does not seem achievable with copper, which dopes CdTe through the formation of substitutional impurities Cu_{Cd}, but it also acts as a donor in interstitial positions. Furthermore, Cu is a fast diffuser in CdTe and is widely considered the primary cause of degradation in these devices [5].

A possible alternative is using Group V elements (N, P, As, Sb, and Bi), which can introduce acceptor states by substituting Te sites [1]. Arsenic appears to be the most widely studied because theoretical studies indicate a good balance between the possibility of forming shallow acceptor states and relatively small formation energy [6]. Moreover, devices with efficiencies of over 20% have been fabricated [7]. In the case of Cu, we have already demonstrated that chlorine is a suitable impurity conveyor for introducing a dopant into CdTe devices [8]. On the other hand, arsenic (III) chloride is lethal even in small doses; it is highly toxic, especially considering its volatility and solubility in water. Antimony is also an excellent candidate;

despite the deeper acceptor level, it can achieve considerable hole density because Sb_{Te} has a smaller formation energy due to the small difference in atomic radii between Te and Sb [6]. However, applying $SbCl_3$ is very inconvenient because the compound is highly hygroscopic, and both the preparation of the solution and its deposition on the sample require a controlled atmosphere. Thus, we have developed an alternative method to dope CdTe with Sb, which does not involve the introduction of highly toxic/lethal compounds or complicated production steps. We have utilized a thin Sb_2Se_3 layer as an Sb source and a subsequent $CdCl_2$ treatment to convey the Sb into the absorber matrix. The advantage of using Sb_2Se_3 is that no other impurities are introduced into the absorber because Se is already present in large quantities in CdSeTe/CdTe devices. Moreover, Sb_2Se_3 can reduce the Schottky barrier at the back contact, and this will be shown in this paper.

2 | Characterization Methods

Raman analyses were performed using a He–Ne laser ($\lambda_{exc} = 633$ nm) coupled to a single-stage Raman spectrometer (Thermo Scientific DXR2) and a thermoelectrically cooled charge-coupled device.

Secondary ion mass spectrometry (SIMS) depth profiles were collected on a CAMECA IMS-4f using a Cs+ primary ion beam with a 14.5-keV ion impact energy and detection of negative secondary ions.

Drive level capacitance profiling (DLCP), capacitance voltage (CV), and admittance spectroscopy (AS) were executed by an HP4284A LCR. The temperature was set by a Janis cryostat with a Lakeshore 325 temperature controller in a vacuum of 10^{-4} Pa and in the range of 90–330 K.

SEM-CL analysis was performed using a xenon dual beam Helios G4 pFIB (plasma focused ion beam). Samples were mounted onto a SEM stub using a conductive carbon/aluminum tab and exposed to sputter deposition of Au/Pd to prevent charge build-up during analysis. The sample was mounted on a pretilted 36° holder. The sample height was set to the eucentric position (the height at which ion and electron beams are incident) and tilted to 16°, providing an overall tilt of 52° to align with the ion column for subsequent milling ~3 μm of Pt was deposited at 16 kV accelerating voltage and a probe current of 10 nA, followed by milling beneath the Pt adjacent to the edge of the sample with an accelerating voltage of 30 kV and a probe current of 60 nA. This provided a smooth, continuous cross-section. Cathodoluminescence was performed in cross-section with Gatan Monarc Pro. Spectrum images were taken in a 250 × 50 pixel area with a step size of 50 nm and an exposure time of 1 s with the spectrometer blazed to 300 lines per mm. The center of the spectrum was set to 800 nm, with a spectral range of 423 nm, where we used a CCD (185–1100 nm). Additionally, NIR emissions were captured over the range of 700–1400 nm with an accelerating voltage of 10 kV and a probe current of 26 nA using a cryogenically cooled InGaAs diode (900–1900 nm).

Current density-voltage (JV) characteristics were measured with a Keithley Source Meter 2420, under an AM 1.5 spectrum at 100 mW/cm^2, using a LOT Quantum Design Europe solar simulator LS0306.

Grazing incidence X-ray diffraction (GXRD) was carried out with a Rigaku diffractometer system with a PhotonMax high-flux 9-kW rotating anode X-ray source, coupled with an XSPA-400ER 2D/1D/0D hybrid pixel array direct photon counting detector.

3 | Device Fabrication

In our laboratory, we fabricate CdSeTe/CdTe devices in superstrate configuration, by following a low substrate temperature deposition method based on thermal evaporation (TE). The substrate and front contact consist of a commercial glass/SnO_2:F (FTO)/SnO_2 (TO) stack (namely TEC 12D) supplied by NSG Pilkington. Once cleaned, TEC 12D substrates are placed in the CdSe-CdTe TE machine and annealed in vacuum. Later, a 300-nm-thick CdSe film followed by a 300-nm-thick CdTe layer, evaporated from CdSe and CdTe granules (99.999% purity), is deposited at a substrate temperature of 340°C. This stack is then annealed at 450°C in vacuum for half an hour before the absorber is completed by depositing another 1.4-μm-thick CdTe layer. The optimization of the absorber layer growth, with a total thickness of 2 μm, has been discussed previously [9]. Subsequently, the stack undergoes a $CdCl_2$ activation treatment performed by a wet deposition method; $CdCl_2$ powder (cadmium chloride monohydrate RE—Pure, from Carlo Erba) is dissolved in methanol, and the solution is drop cast on the surface, followed by annealing in air at 400°C for 1 h. After this treatment, the stack is dipped in boiling water to remove $CdCl_2$ residues and to clean the surface. Then, the doping process begins (see Figure 1): A 10-nm-thick Sb_2Se_3 layer is deposited onto the sample by TE from Sb_2Se_3

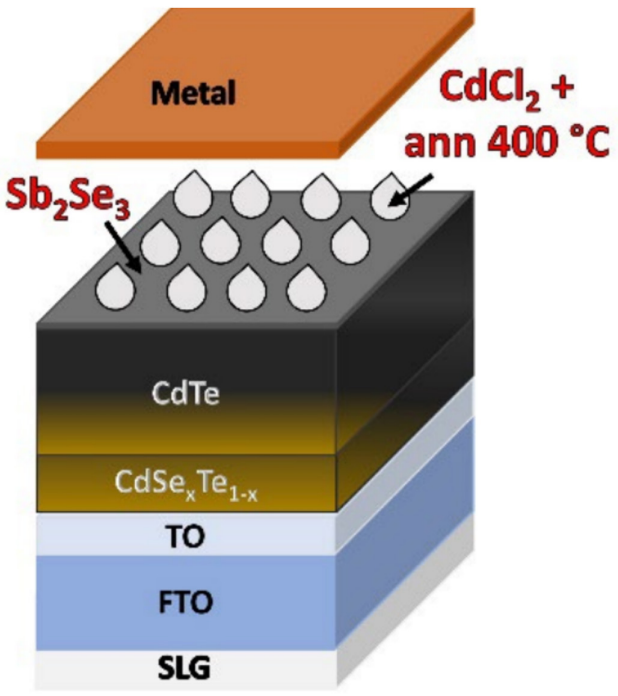

FIGURE 1 | Schematic of the CdTe Sb-doping process.

granules (99.999% purity), at a substrate temperature of 300°C. Subsequently, the sample is annealed at 400°C in vacuum. Then, the $CdCl_2$ treatment is repeated on the sample, with an annealing time of 30 min, followed by cleaning the surface in boiling water. Finally, as a back contact, a 30-nm-thick gold layer (99.99% purity) is deposited by TE.

On the other hand, in the case of copper doping, a 1-nm-thick Cu layer (99.999% purity) is deposited onto the sample by TE after the first activation treatment. Before its deposition, the sample undergoes a Br-MeOH etch to clean the surface and, mainly, to enrich the absorber surface in Te. This favors the formation of Cu_xTe compounds at the back contact, improving its ohmic behavior and stability [8, 10]. Again, the back contact consists of a 30-nm-thick gold layer, but, in this case, the sample is then annealed at 200°C in air to diffuse Cu into the absorber.

4 | Optimization of the Fabrication Process

After Sb_2Se_3 deposition at a substrate temperature of 300°C, annealing in vacuum at 400°C significantly increases the efficiency of the devices. The idea behind this was to improve the crystallinity of the layer and expose it to the activation treatment temperature before the deposition of the $CdCl_2$ solution. Sb_2Se_3 does not deposit/reevaporate if grown by TE at a higher substrate temperature.

To characterize the structure of such a thin layer, Raman spectroscopy has been performed on the Sb_2Se_3 surface before and after the annealing at 400°C and after the subsequent $CdCl_2$ treatment (Figure 2).

The as-deposited film shows Raman modes around 119, 154, 192, and 208 cm^{-1}, revealing an orthorhombic Sb_2Se_3 structure [11]. In particular, the vibration at 119 cm^{-1} is related to the Se–Se and 154 cm^{-1} to the Sb–Sb bonds in (Se_2Sb–$SbSe_2$) structural units, whereas the prominent peaks at 192 and 208 cm^{-1} are associated with the A_g mode of the Sb–Se–Sb bending vibrations [12].

After annealing, Raman shows only the peak at 208 cm^{-1}, confirming that Sb_2Se_3 is still present on the surface but recrystallized. By comparing the normalized spectra, this peak becomes sharper, pointing out an improved crystallinity of the layer. Moreover, two peaks at 143 and 166 cm^{-1}, related to CdTe, are detected, suggesting a possible thinning of the Sb_2Se_3 film. The first mode is attributable to the overlap of transverse optical phonon signals of CdTe and elementary Te, whereas the second is due to the longitudinal optical phonon of CdTe.

After Sb_2Se_3 undergoes the $CdCl_2$ treatment, only two modes around 122 and 141 cm^{-1} are detected, which are ascribed to the vibrations of the A_1 mode of elemental Te and a shift of the previous 143 cm^{-1} peak, respectively [13, 14]. Thus, the treatment thoroughly mixes the Sb_2Se_3 with the underlying CdTe layer. Moreover, the process seems to produce a Te-rich CdTe surface, which would be beneficial to the devices because it would improve the electrical properties of the back contact, allowing a decrease in the potential barrier [15].

To test whether $CdCl_2$ treatment actually enhances the diffusion of Sb into the devices, SIMS analysis has been performed on the samples before and after the activation treatment.

Figure 3 shows the distribution profiles of Se and Sb in the samples before (in black) and after (in red) the activation treatment. Before $CdCl_2$, SIMS clearly shows the presence of Sb and Se on the sample surface, which rapidly decreases below the detection level for Sb, moving towards the bulk. Also, Se and Sb signals have similar profiles, suggesting that they are bonded in a compound, as seen from Raman analysis. This indicates poor decomposition of the Sb_2Se_3 after the 400°C annealing and poor diffusion of the elements.

However, after the $CdCl_2$ treatment, the concentration of Sb on the surface is reduced, and its profile shows a higher signal towards

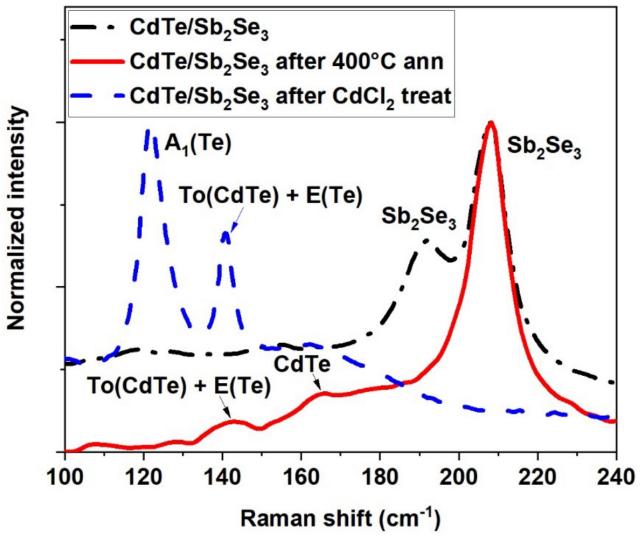

FIGURE 2 | Raman spectra (in the 100–240 cm^{-1} range) of Sb_2Se_3 on CdTe: as-deposited, after vacuum annealing at 400°C, and after $CdCl_2$ activation treatment.

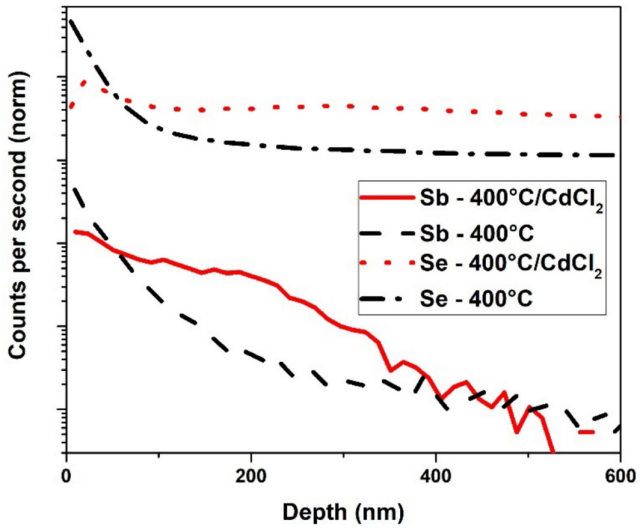

FIGURE 3 | SIMS depth profiles showing Se and Sb distribution from the back contact (0 nm) to the bulk (600-nm depth from the surface), before (black) and after (red) the $CdCl_2$ treatment.

the bulk, demonstrating its diffusion into the absorber. At a depth of 400 nm, the Sb signal goes below the detection level, showing that its distribution is not homogeneous but that a more significant quantity remains near the back contact. Instead, for Se, apart from a small peak on the surface, which can be attributed to a measurement artifact, the profile is completely flattened. The small amount of Se added with the application of Sb_2Se_3 does not appear to substantially alter the initial concentration given by the CdSe introduction. The difference in counts per second between the Se profiles of the two samples cannot be considered relevant. Even if, to facilitate the comparison, the counts have been normalized on the respective flat Te profile of each sample, the profile's trend and not the absolute values are the significant information. However, this analysis indicates that the annealing at 400°C in vacuum is inefficient in doping CdTe; to diffuse and insert Sb in the absorber matrix, the additional treatment with $CdCl_2$ is needed. Sb has a lower diffusion coefficient compared to Cu [16, 17], and in this case, it is also bonded to Se; therefore, more aggressive conditions are required to incorporate the dopant. It is well known that the $CdCl_2$ treatment induces and improves the recrystallization of the CdTe film and enhances the diffusion of S and Te in CdS/CdTe [18] and of Se and Te in CdSeTe/CdTe [19] devices. Furthermore, it has been demonstrated that a post-annealing treatment with chloride (in that case, $SbCl_3$) promotes the recrystallisation of the Sb_2Se_3 film [20]. The presence of chlorine, therefore, promotes the simultaneous recrystallization of the Sb_2Se_2 and CdTe films and improves the elements' diffusion, thus favoring the mixing of the two layers and the incorporation of the dopant. Moreover, Polivtseva et al. [20] prove that the slight Se deficiency observed in Sb_2Se_3 as-deposited films disappears after the $SbCl_3$ treatment, suggesting that chlorine tends to bind to antimony; assuming the same behavior on our samples, this further promotes Sb diffusion at low temperatures [21].

As described above, the Sb distribution in the absorber is not homogeneous, which also suggests a graded doping level from the back contact towards the bulk. This is not a priori a negative factor, and, indeed, it follows the doping profile most often used with copper in CdTe; in fact, Cu has been introduced into CdTe mainly (as for our Cu-doped devices) by diffusion from the back contact: either by depositing pure Cu or by forming CuTe compounds via etching [10] or by directly depositing copper-containing compounds such as ZnTe:Cu [22]. However, this is often considered the desirable dopant depth profile, because an increased carrier concentration at the back side of CdTe results in a reduced back-barrier at the CdTe/metal interface, thereby lowering the recombination rate [8, 23, 24].

5 | Doping and Identification of Defects

To understand if the diffusion of Sb into the absorber leads to CdTe doping, capacitance-voltage and drive-level capacitance profiling analyses have been performed on the completed devices (Figure 4).

CV profiles show the contribution of both deep and shallow defects, whereas the deeper states barely affect the DLCP curves [25]; thus, the net charge density of the samples is usually estimated by the lowest part of the DLCP curve. The arrows in the graphs indicate the measurements at 0 V; these points give us an idea of the depletion region width. Figure 4 shows that, by performing the measurements at both 10 kHz and 1 MHz, the samples containing Sb_2Se_3 but without the subsequent $CdCl_2$ treatment have the same net charge density as the undoped samples. This confirms what was suggested by SIMS analysis: The annealing at 400°C of the Sb_2Se_3/CdTe stack is inefficient in doping CdTe.

However, in the case of treated Sb_2Se_3 at 10 kHz, the samples show an increased net charge density, indicating that, in this case, Sb is acting as a dopant. However, the net charge density results are lower than those of the Cu-doped devices. Things are reversed when the measurement is performed at a frequency of 1 MHz. This suggests the presence of different dominant acceptors in the two cells, probably shallower for the Sb-doping case, because the higher the frequency, the lower the response of deeper defects [26]. Furthermore, all the devices have the CV profiles below the DLCP ones, indicating that the deep defects are donors. This is corroborated by the increase of the CV profiles at 1 MHz compared to 10 kHz: At a higher frequency, the

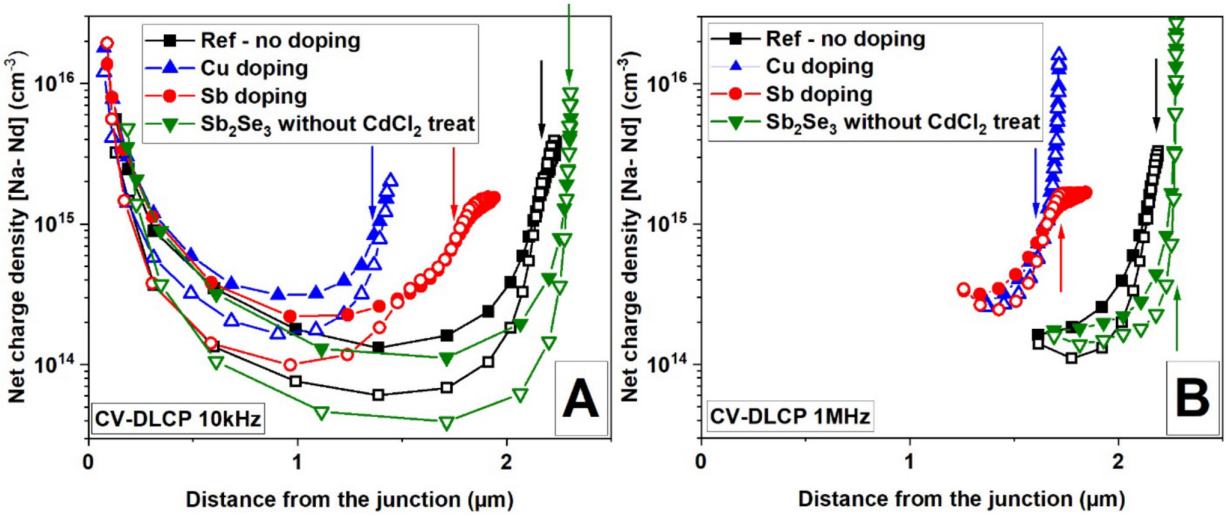

FIGURE 4 | Comparison between CV (open dots) and DLCP (full dots) measurements done at 10 kHz (A) and 1 MHz (B) at room temperature of a reference sample (no doping), cells doped with Cu and Sb (Sb_2Se_3 with $CdCl_2$ treatment), and a sample with Sb_2Se_3 without $CdCl_2$ treatment.

response of the deeper donors is lower [26]. Thus, there is less compensation, and the net charge densities result higher.

To identify the nature of the different defects seen by CV-DLCP measurements, admittance spectroscopy has been conducted on Sb-doped samples ($CdTe/Sb_2Se_3 + CdCl_2$ treatment) and compared with the results on our Cu-doped devices [9].

TABLE 1 | List of defects identified by AS.

Cu-doped [9]			Sb-doped	
Ea **(meV)**	***σa*** **(cm^{-2})**	**Defect**	***Ea*** **(meV)**	***σa*** **(cm^{-2})**
107 ± 2	$5\ 10^{-16}$	A	122 ± 5	$3\ 10^{-15}$
		B	266 ± 8	$6\ 10^{-16}$
336 ± 1	$2\ 10^{-14}$	C		
352 ± 6	$3\ 10^{-15}$			

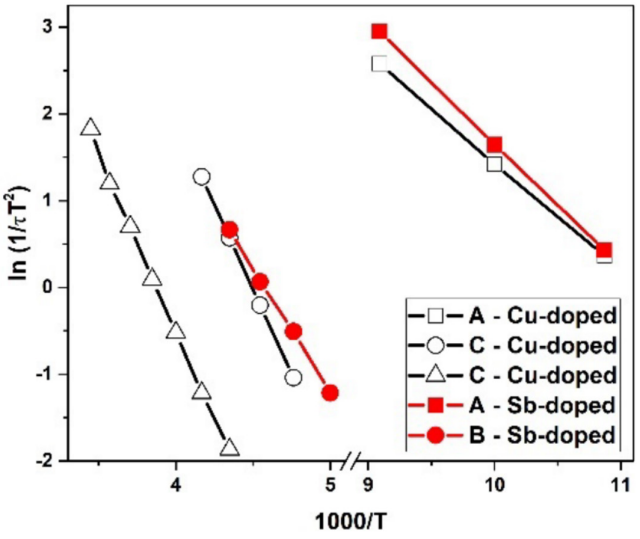

FIGURE 5 | Arrhenius plot of the admittance spectroscopy data obtained from Cu- and Sb-doped samples (with A–C identified defects).

In Sb-doped devices, two dominant defects have been detected at (122 ± 5) and (266 ± 8) meV. The first (A) can be attributed to an A-center, a single acceptor formed by a V_{Cd}-Cl_{Te} complex [27] (see Table 1 and Figure 5), which is present in all our samples. Instead, the second defect has an activation energy (*Ea*) that differs from those usually identified in Cu-doped samples, thus suggesting its relation to Sb introduction. The *Ea* of this defect is in good agreement with those already measured in Sb-doped CdTe crystals and attributed to Sb_{Te} centers [28, 29]. Also, this value is close to that predicted for the Sb_{Te} point defect using first-principles band structure methods [30]. These defects act as acceptors, doping CdTe; they cannot be adequately defined as shallow, but they are closer to the valence band than the defects C. These last ones are detected only in Cu-doped devices, and they are generally attributed to the Cu at Cd substitutional sites, generating deep acceptors that are believed to increase the p-type doping [31, 32].

Sb-doped samples have been further characterized by cathodoluminescence spectroscopy. Figure 6A presents the emission spectrum acquired from the absorber in cross-section; the points where the measurements were taken were identified with SEM microscopy (Figure 6B). The analysis highlights a prominent emission peak at 875 nm, corresponding to an energy of 1.42 eV and thus attributable to an interband transition. At longer wavelengths, a second broader peak is observed, centered at 1020 nm, coinciding with an emission energy of 1.22 eV. This peak occurs only in antimony-doped samples, and it is consistent with a transition between the free electron and an energy level associated with an acceptor about 200 meV above the valence band. This activation energy is close to that estimated from the AS measurements and previously attributed to Sb^-_{Te} centers [28–30], corroborating the effective doping of the CdSeTe/CdTe absorber with antimony.

6 | Performance of the Devices

Regarding the performance of the devices, Sb-doped cells demonstrate a slightly lower average efficiency compared to Cu-doped, around 1% less (see Table 2). This is due to a slight reduction of all the average efficiency parameters, even if the

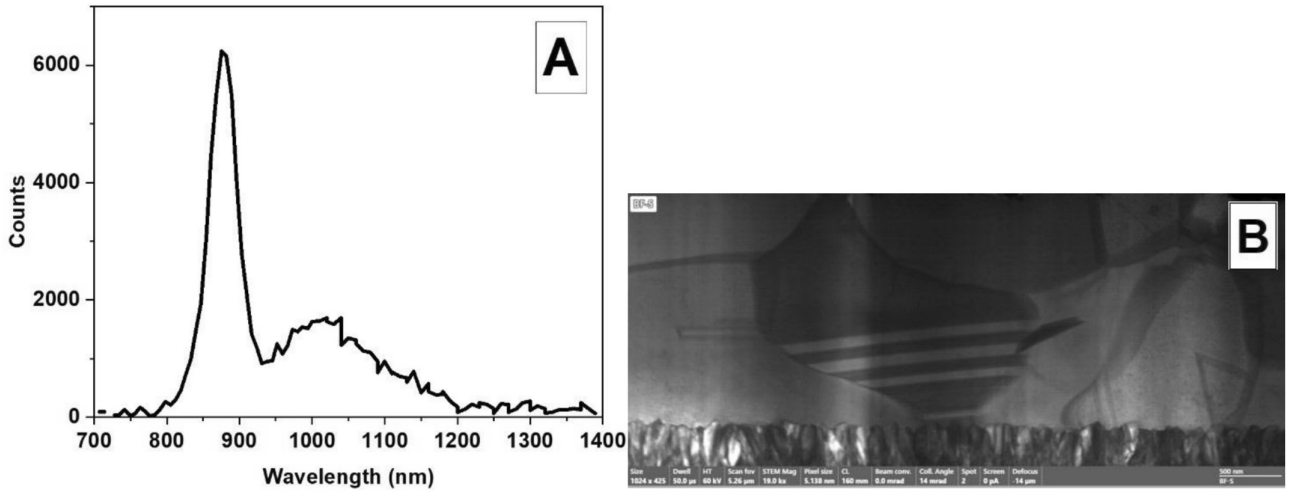

FIGURE 6 | (A) cathodoluminescence spectra (in the 700- to 1400-nm range) taken from the cross-section of the absorber of Sb-doped samples. (B) Cross-sectional SEM image of the CdSeTe/CdTe absorber.

values are equal within the error limit. For both samples, the average current densities near 28 mA/cm^2 (also confirmed by EQE analysis) are very good considering the absorber thickness of 2 μm; to our knowledge, these current values are the highest registered for 2-μm-thick CdTe-based devices. Moreover, achieving efficiencies almost equal to those with Cu by application of Sb_2Se_3 is very promising, considering that Cu doping has been optimized over the years, whereas these Sb-doped results are mostly preliminary.

Moreover, the record devices presented in Table 3 show very close efficiencies: 15.7% versus 15.4% for Cu and Sb doping, respectively, with similar J-V parameters, demonstrating the potential of the Sb_2Se_3 layer in doping CdTe. The discrepancy between average values and peak efficiencies also corroborates the idea that the slightly lower performance of the Sb-doped samples is primarily due to an incomplete optimization of the Sb-doping process.

Figure 7 displays the current–voltage characteristics of the above-mentioned Cu- and Sb-doped record devices: As expected, the curves almost overlap. But the most noticeable difference is in the first quadrant of the graph: The Cu-doped device shows a slight rollover effect, whereas the Sb-doped presents a more ohmic back contact. This is quite surprising because, in the Cu-doping process, the sample undergoes a Br-MeOH etching to enrich the CdTe surface in Te and favors the formation of Cu_xTe compounds [8]. These are generated to improve the ohmicity of the back contact and the stability of the cells [10, 33]. In the case of the Sb-doping process, given the absence of copper, after $CdCl_2$ treatment the surface is simply cleaned in distilled water. However, Raman analysis indicates that the $CdCl_2$ treatment performed on the Sb_2Se_3 layer creates a Te-rich CdTe surface despite the lack of an etching process. As mentioned, a Te-rich surface is beneficial because it decreases the potential barrier at the back contact [15]. Indeed, the JV characteristics of the Sb-doped cells suggest that this Te-enrichment effectively improves the ohmicity of the back contact.

To further investigate the back contact of the devices, grazing incidence XRD has been performed on the surface of the finished cells to analyze the surface of the absorber (see Figure 8). The measurements have been carried out using an X-ray beam incidence angle of 0.5° to study only the first few nanometers of the material. As expected, Cu- and Sb-doped samples show peaks attributable to CdTe and Au. Moreover, both present peaks related to TeO_2 (approximately at 15°, 30°, 31°, and 34°) [34], but much more intense for the Sb case in the 30°–35° region. Recently, TeO_2 has been applied at the back contact of CdSeTe/CdTe devices as a passivation layer, with the idea of reducing surface recombination rates and increasing carrier lifetimes; the studies suggest that this layer may favorably bend the energy bands at the back of the cells, promoting hole collection and reducing recombination at the back interface [35–37]. Furthermore, the Sb-doped samples also demonstrate the presence of Sb_2Se_3 compound with (110) and (220) orientations (JCPDS Card No. PDF 150861). Theoretically, because Sb_2Se_3 has both a lower electron affinity and band gap than CdTe, the Schottky barrier between Sb_2Se_3 and Au is smaller than that between CdTe and Au. Indeed, from our experience on Sb_2Se_3 solar cells [38], the absorber-Au back contact shows good ohmicity without roll-over effect, which is not the case for CdTe-Au, where adding copper

TABLE 2 | average efficiency parameters of devices.

Devices	Voc (mV)	Jsc (mA/cm^2)	FF (%)	η (%)
Cu doped	808 ± 18	27.9 ± 0.8	69 ± 2	15.5 ± 0.5
Sb doped	797 ± 6	27.5 ± 0.8	66 ± 1	14.6 ± 0.6

TABLE 3 | Efficiency parameters of record devices (JV curves in Figure 4).

Devices	Voc (mV)	Jsc (mA/cm^2)	FF (%)	η (%)
Cu doped	790	28.7	69	15.7
Sb doped	797	28.4	68	15.4

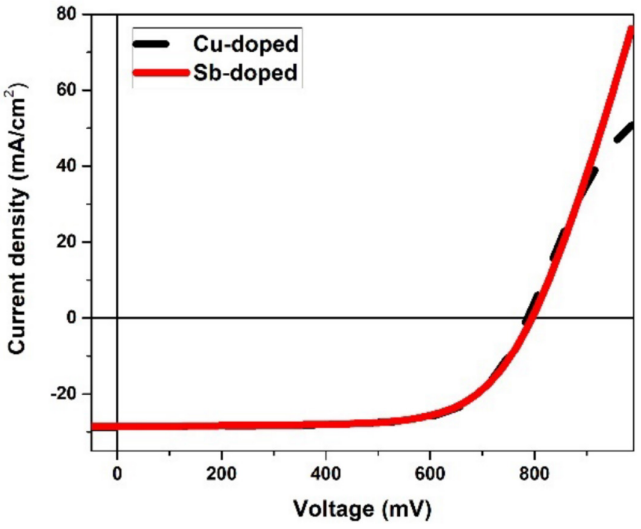

FIGURE 7 | Current density-voltage curves of the record Cu- and Sb-doped CdTe devices (efficiency parameters in Table 3).

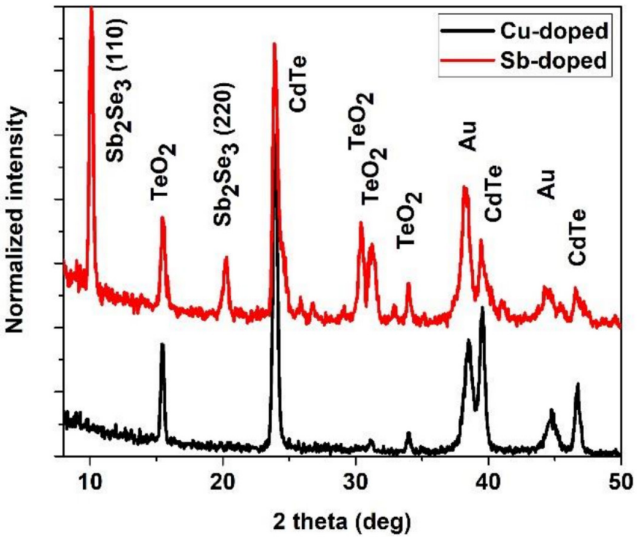

FIGURE 8 | Comparison of GXRD spectra (in the 8–50 two theta degrees range) collected at the back contact of Cu- and Sb-doped devices.

compounds or forming a p+ layer at the rear absorber surface is needed [8]. Consequently, in principle, Sb_2Se_3 at the back contact of CdTe devices could reduce the back contact barrier and would favor carrier extraction, explaining, together with the more significant amount of TeO_2, the absence of a rollover. In summary, Sb_2Se_3 as well as TeO_2 would favor the band alignment, and, in addition, TeO_2 would also provide a passivation effect.

7 | Stability of the Cells

To test the degradation of the samples over time, Cu- and Sb-doped samples have been subjected to accelerated stress tests (AST). Additionally, samples without any doping have also been tested for comparison. In particular, the cells have been kept in a specific metal chamber, under an illumination of 1 Sun at a temperature of 80°C without any encapsulation. The cells have been aged for about 300 h; at specific time intervals, the samples were removed from the chamber, cooled down, and measured under the solar simulator. Figure 9 shows the efficiency of the devices, normalized to their initial efficiency, at different time steps of AST.

Regarding the copper-doped samples, the results align with what we have already reported for our copper-doped devices with CdS/CdTe structure [5, 8]. After about 75 h, the average efficiency drops to around 80% of the initial value and decreases to less than 65% in just over 250 h. This degradation is attributed to the diffusion of Cu from the back contact towards the junction and to the instability of the Cu_{Cd} acceptor defects [5]. Indeed, this is supported by the much higher stability of the undoped cells; after more than 250 h of aging, the undoped devices show about 90% of their initial efficiency. In this case, the degradation can be attributed to the exposure of the devices to moisture and oxygen.

For Sb-doped devices, after over 250 h of aging, these devices maintain, on average, 90% of their initial efficiency, in line with the undoped samples. Therefore, we can assume that, again, the degrading factors are moisture and oxygen, concluding that the acceptor defects due to the introduction of Sb, unlike those due to Cu, are stable.

To analyze which parameters determine the reduction in efficiency, Figure 10 reports the FF, Voc, and Jsc of the devices, normalized to their initial values, at different time steps of AST. The graphs

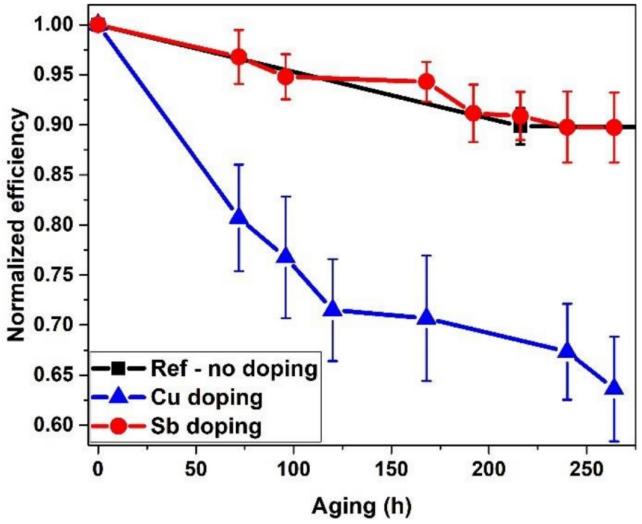

FIGURE 9 | Graph reporting the performance degradation over time of Cu- and Sb-doped samples and the reference no-doped cells. Results concerned the normalized efficiency at different time steps of AST.

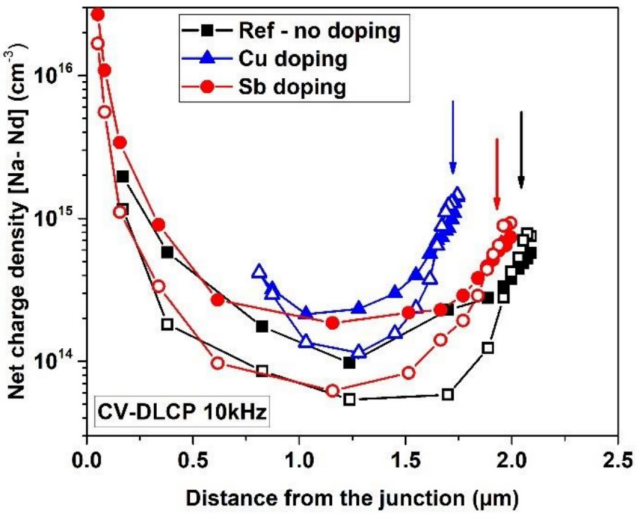

FIGURE 11 | Comparison between CV (open dots) and DLCP (full dots) measurements, done at 10 kHz at room temperature, of reference (no doping), Cu- and Sb-doped samples after AST.

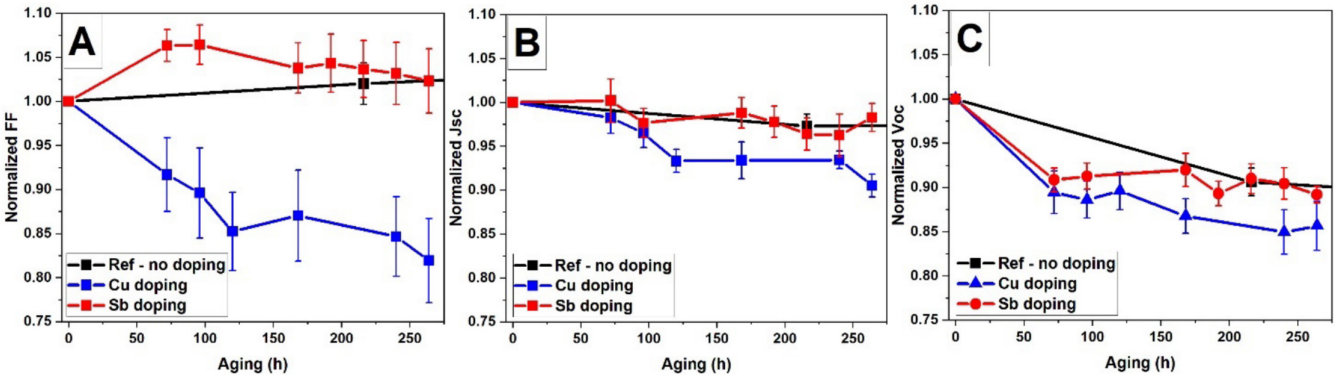

FIGURE 10 | Graph reporting the performance degradation over time of Cu- and Sb-doped samples and the reference no-doped cells. Results concerned the normalized FF (A), Jsc (B), and Voc (C) at different time steps of AST.

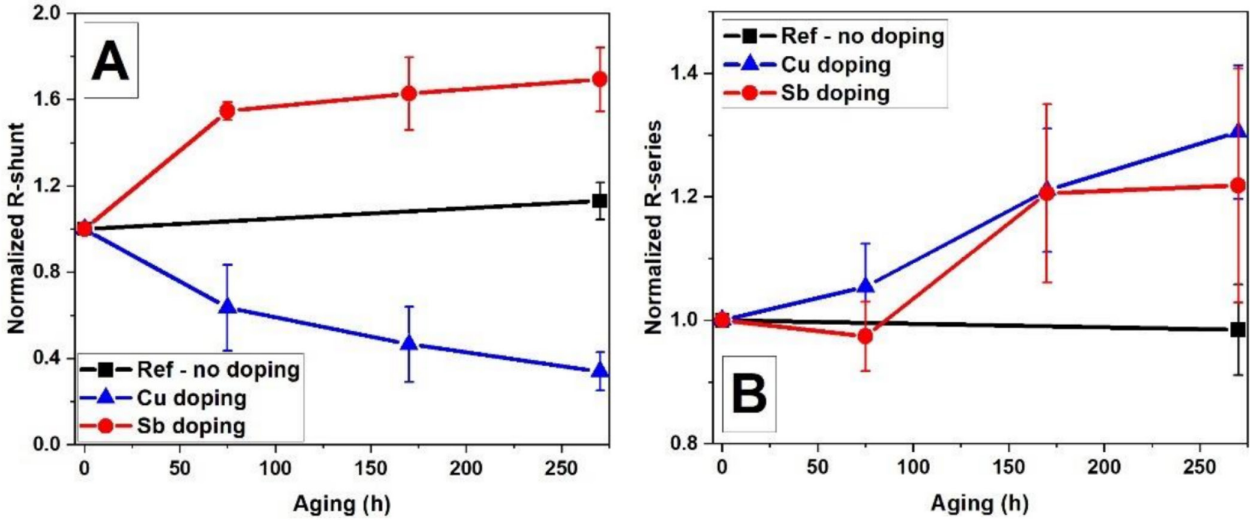

FIGURE 12 | Graph reporting normalized shunt (A) and series (B) resistances during AST of the Cu- and Sb-doped and reference cells.

show that the current density is relatively stable for all the samples, with only a slight decrease for the Cu-doped cells, with Jsc around 92% at 250 h of AST. Regarding Voc, Sb-doped and reference cells have the same decline to around 90%, whereas the Cu-doped devices decline to 85%. A lower Voc can be partly due to reduced net charge density. To check this, CV-DLCP measurements have been repeated on the samples after AST (see Figure 11). All the devices demonstrate a decrease in net charge density, which explains the larger depletion region width (indicated by the colored arrow for each sample) compared to the cells before the stress test.

The decrease of the DLCP curves for reference and Sb-doped samples is similar. Instead, although, for the freshly fabricated cells, the DLCP profiles measured at 10 kHz of the Cu-doped are higher than the Sb-doped (see Figure 4A), after AST, the DLCP profiles of the Sb- and Cu-doped devices almost overlap, confirming a more significant net charge density reduction in the presence of copper. These data support the hypothesis that Sb doping, unlike Cu doping, does not introduce additional unstable acceptor defects. Finally, reference and Sb-doped cells show a slight increase in FF over time. On the other hand, the FF drop seems to be the driving factor of the degradation of Cu-doped cells; the average FF decreases to about 82% in 250 h. This is attributed to the diffusion of Cu towards the junction. Cu can segregate into the grain boundaries, causing shunt paths, and its reduced presence at the back contact increases the barrier, leading to a decrease in shunt resistance and an increase in series resistance, resulting in a lower FF [5]. To verify this, series and shunt resistances have been monitored during the AST (see Figure 12), and indeed, Cu-doped cells demonstrate a rise of the series and a substantial reduction of the shunt resistance after the accelerated aging. The resistances are stable over time for the references, whereas Sb-doped cells register an increase in the series (however, lower than for the Cu case) but also a substantial increase in the shunt resistance.

8 | Conclusions

A new method to Sb-dope CdSeTe/CdTe devices has been developed, in particular, by the deposition of a thin Sb_2Se_3 layer onto the CdTe surface and subsequent $CdCl_2$ treatment at 400°C, driving the Sb into the absorber matrix. Choosing Sb_2Se_3 as a doping carrier does not introduce any foreign elements into the absorber, and it reduces the Schottky barrier at the back contact.

This method leads to an effective doping of CdTe, as demonstrated by CV-DLCP measurements, and to peak efficiencies very close to those obtained with Cu doping through the same low-temperature deposition process, 15.4% vs. 15.7%. Also, with Sb_2Se_3, the back contact of doped cells is improved compared to Cu-doped ones, and it does not need any etching or hole transport layer in the fabrication process.

Accelerated stability tests show remarkable stability for Sb_2Se_3-doped solar cells. Sb-containing devices are so stable that their minimum degradation is equal to that of the undoped cells, suggesting that it is only due to the lack of encapsulation.

This innovative doping method has proven to be effective in fabricating Sb-doped CdTe devices with efficiencies similar to Cu-doped cells but with noteworthy stability. However, compared to the well-known Cu doping methods, this new process is still in its preliminary state, so it could also offer significant room for improvement. Finally, this simple postabsorber deposition process has a very strong potential to be applied to any CdTe device fabricated by any deposition technique.

Author Contributions

Elisa Artegiani: writing – review and editing, conceptualization, methodology, investigation, validation, visualization. **Andrea Gasparotto:** investigation, formal analysis, visualization. **Sam Machin:** methodology, investigation, formal analysis. **Michael Walls:** writing – review and editing, conceptualization, methodology, supervision. **Alessandro Romeo:** writing – review and editing, conceptualization, methodology, visualization, supervision, project administration.

Acknowledgments

The Technological Platform Center (CPT) at the University of Verona, in the person of Dr. Marco Giarola, is thankfully acknowledged for Raman and XRD measurements. The Loughborough authors are

grateful to EPSRC through Project EP/X030245/1 for funding to install the cathodoluminescence facility. Open access publishing facilitated by Universita degli Studi di Verona, as part of the Wiley - CRUI-CARE agreement.

Funding

This work was supported by the Italian Ministry of University and Research (MUR) through the PON "Research and Innovation" 2014–2020, D.M. 1062/2021 (Action IV.4/IV.6), with REACT-EU/European Social Fund resources: CUP: B39J21025850001.

References

1. M. A. Scarpulla, B. McCandless, A. B. Phillips, et al., "CdTe-Based Thin Film Photovoltaics: Recent Advances, Current Challenges and Future Prospects," *Solar Energy Materials and Solar Cells* 255 (2023): 112289, https://doi.org/10.1016/j.solmat.2023.112289.

2. R. Meagley, C. McIntosh, B. Bob, C. Ellis, L. Tinker, and M. Beck, "Cadmium Telluride Photovoltaics Perspective Paper," 2025. [Online], https://www.energy.gov/sites/default/files/2025-01/DOE%20SETO%20CdTe%20Photovoltaics%20Perspective%20Paper.pdf.

3. N. R. Paudel and Y. Yan, "Enhancing the Photo-Currents of CdTe Thin-Film Solar Cells in Both Short and Long Wavelength Regions," *Applied Physics Letters* 105, no. 18 (2014): 1–6, https://doi.org/10.1063/1.4901532.

4. J. Guo, A. Mannodi-Kanakkithodi, F. G. Sen, et al., "Effect of Selenium and Chlorine Co-Passivation in Polycrystalline CdSeTe Devices," *Applied Physics Letters* 115, no. 15 (2019): 153901, https://doi.org/10.1063/1.5123169.

5. E. Artegiani, J. D. Major, H. Shiel, V. Dhanak, C. Ferrari, and A. Romeo, "How the Amount of Copper Influences the Formation and Stability of Defects in CdTe Solar Cells," *Solar Energy Materials and Solar Cells* 204 (2020): 110228, https://doi.org/10.1016/j.solmat.2019.110228.

6. B. Dou, Q. Sun, and S. H. Wei, "Optimization of Doping CdTe With Group-V Elements: A First-Principles Study," *Physical Review Applied* 15, no. 5 (2021): 054045, https://doi.org/10.1103/PhysRevApplied.15.054045.

7. W. K. Metzger, S. Grover, D. Lu, et al., "Exceeding 20% Efficiency With In Situ Group V Doping in Polycrystalline CdTe Solar Cells," *Nature Energy* 4, no. 10 (2019): 837–845, https://doi.org/10.1038/s41560-019-0446-7.

8. E. Artegiani, D. Menossi, H. Shiel, et al., "Analysis of a Novel CuCl2 Back Contact Process for Improved Stability in CdTe Solar Cells," *Progress in Photovoltaics: Research and Applications* 27, no. 8 (2019): 706–715, https://doi.org/10.1002/pip.3148.

9. E. Artegiani, A. Gasparotto, M. Meneghini, G. Meneghesso, and A. Romeo, "How the Selenium Distribution in CdTe Affects the Carrier Properties of CdSeTe/CdTe Solar Cells," *Solar Energy* 260 (2023): 11–16, https://doi.org/10.1016/j.solener.2023.05.058.

10. X. Wu, J. Zhou, A. Duda, et al., "Phase Control of CuxTe Film and Its Effects on CdS/CdTe Solar Cell," *Thin Solid Films* 515, no. 15 SPEC. ISS (2007): 5798–5803, https://doi.org/10.1016/j.tsf.2006.12.151.

11. A. Shongalova, M. R. Correia, B. Vermang, J. M. V. Cunha, P. M. P. Salomé, and P. A. Fernandes, "On the Identification of Sb2Se3 Using Raman Scattering," *MRS Communications* 8, no. 3 (2018): 865–870, https://doi.org/10.1557/mrc.2018.94.

12. A. Kumar, V. Kumar, A. Romeo, C. Wiemer, and G. Mariotto, "Raman Spectroscopy and In Situ XRD Probing of the Thermal Decomposition of Sb2Se3 Thin Films," *Journal of Physical Chemistry C* 125, no. 36 (2021): 19858–19865, https://doi.org/10.1021/acs.jpcc.1c05047.

13. V. Vozda, T. Burian, J. Chalupský, et al., "Micro-Raman Mapping of Surface Changes Induced by XUV Laser Radiation in Cadmium Telluride," *Journal of Alloys and Compounds* 763 (2018): 662–669, https://doi.org/10.1016/j.jallcom.2018.05.332.

14. S. S. Islam, S. Rath, K. P. Jain, S. C. Abbi, C. Julien, and M. Balkanski, "Forbidden One-LO-Phonon Resonant Raman Scattering and Multiphonon Scattering in Pure CdTe Crystals," *Physical Review B* 46, no. 8 (1992): 4982–4985, https://doi.org/10.1103/PhysRevB.46.4982.

15. J. Sarlund, M. Ritala, M. Leskelä, E. Siponmaa, and R. Zilliacus, "Characterization of Etching Procedure in Preparation of CdTe Solar Cells," *Solar Energy Materials and Solar Cells* 44, no. 2 (1996): 177–190, https://doi.org/10.1016/0927-0248(96)00053-0.

16. H. Zhao, T. M. Razykov, D. Hodges, A. Farah, C. S. Ferekides, and D. Morel, "Introduction of Sb in CdTe and Its Effect on CdTe Solar Cells," in Conference Record of the IEEE Photovoltaic Specialists Conference, (2008). https://doi.org/10.1109/PVSC.2008.4922554.

17. J. N. Duenow, E. Colegrove, J.-H. Yang, et al., "Experimental and Theoretical Comparison of Sb, As, and P Diffusion Mechanisms and Doping in CdTe," *Journal of Physics D: Applied Physics* 51, no. 7 (2018): 075102, https://doi.org/10.1088/1361-6463/aaa67e.

18. B. E. McCandless, L. V. Moulton, and R. W. Birkmire, "Recrystallization and Sulfur Diffusion in CdCl2-Treated CdTe/CdS Thin Films," *Progress in Photovoltaics: Research and Applications* 5, no. 4 (1997): 249–260, https://doi.org/10.1002/(sici)1099-159x(199707/08)5:4<249::aid-pip178>3.0.co;2-s.

19. A. H. Munshi, J. M. Kephart, A. Abbas, et al., "Effect of CdCl2 Passivation Treatment on Microstructure and Performance of CdSeTe/CdTe Thin-Film Photovoltaic Devices," *Solar Energy Materials and Solar Cells* 186, no. May (2018): 259–265, https://doi.org/10.1016/j.solmat.2018.06.016.

20. S. Polivtseva, J. O. Adegite, J. Kois, et al., "A Novel Thermochemical Metal Halide Treatment for High-Performance Sb2Se3 Photocathodes," *Nanomaterials* 11, no. 1 (2021): 1–14, https://doi.org/10.3390/nano11010052.

21. D. B. Li, C. Yao, S. N. Vijayaraghavan, et al., "Low-Temperature and Effective Ex Situ Group V Doping for Efficient Polycrystalline CdSeTe Solar Cells," *Nature Energy* 6, no. 7 (2021): 715–722, https://doi.org/10.1038/s41560-021-00848-z.

22. T. A. Gessert, A. R. Mason, P. Sheldon, A. B. Swartzlander, D. Niles, and T. J. Coutts, "Development of Cu-Doped ZnTe as a Back-Contact Interface Layer for Thin-Film CdS/CdTe Solar Cells," *Journal of Vacuum Science & Technology A: Vacuum, Surfaces, and Films* 14, no. 3 (1996): 806–812, https://doi.org/10.1116/1.580394.

23. C. R. Corwine, A. O. Pudov, M. Gloeckler, S. H. Demtsu, and J. R. Sites, "Copper Inclusion and Migration From the Back Contact in CdTe Solar Cells," *Solar Energy Materials and Solar Cells* 82 (2004): 481–489, https://doi.org/10.1016/j.solmat.2004.02.005.

24. D. B. Li, S. S. Bista, Z. Song, et al., "Maximize CdTe Solar Cell Performance Through Copper Activation Engineering," *Nano Energy* 73 (2020): 104835, https://doi.org/10.1016/j.nanoen.2020.104835.

25. J. T. Heath, J. D. Cohen, and W. N. Shafarman, "Bulk and Metastable Defects in CuIn1-xGaxSe2 Thin Films Using Drive-Level Capacitance Profiling," *Journal of Applied Physics* 95, no. 3 (2004): 1000–1010, https://doi.org/10.1063/1.1633982.

26. J. T. Heath, J. D. Cohen, and W. N. Shafarman, "Distinguishing Metastable Changes in Bulk CIGS Defect Densities From Interface Effects," *Thin Solid Films* 431-432 (2003): 426–430, https://doi.org/10.1016/S0040-6090(03)00189-5.

27. A. Castaldini, A. Cavallini, B. Fraboni, P. Fernandez, and J. Piqueras, "Comparison of Electrical and Luminescence Data for the A Center in CdTe," *Applied Physics Letters* 69 (1996): 3510–3512.

28. Y. Iwamura, S. Yamamori, H. Negishi, and M. Moriyama, "Deep Levels of High Resistivity Sb Doped CdTe," *Japanese Journal of Applied Physics* 24, no. 3 (1985): 361–362, https://doi.org/10.1143/JJAP.24.361.

29. P. Fochuk, R. Grill, Y. Nykonyuk, et al., "High Temperature Properties of CdTe Crystals, Doped by Sb," *IEEE Transactions on Nuclear Science* 54 (2007): 763–768, https://doi.org/10.1109/TNS.2007.902368.

30. S. H. Wei and S. B. Zhang, "Chemical Trends of Defect Formation and Doping Limit in II–VI Semiconductors: The Case of CdTe," *Physical Review B: Condensed Matter and Materials Physics* 66, no. 15 (2002): 1–10, https://doi.org/10.1103/PhysRevB.66.155211.

31. J. Beach, F. H. Seymour, V. I Kaydanov, and T. R. Ohno, "Studies of Basic Electronic Properties of CdTe-Based Solar Cells and Their Evolution During Processing and Stress," Annual Technical Report, 1 November 2005–31 October 2006 (2005).

32. A. Balcioglu, R. K. Ahrenkiel, and F. Hasoon, "Deep-Level Impurities in CdTe/CdS Thin-Film Solar Cells," *Journal of Applied Physics* 88, no. 12 (2000): 7175–7178, https://doi.org/10.1063/1.1326465.

33. I. Rimmaudo, A. Salavei, E. Artegiani, et al., "Improved Stability of CdTe Solar Cells by Absorber Surface Etching," *Solar Energy Materials and Solar Cells* 162 (2017): 127–133, https://doi.org/10.1016/j.solmat.2016.12.044.

34. B. Lafuente, R. T. Downs, H. Yang, and N. Stone, "The Power of Databases: The RRUFF Project," in *Highlights in Mineralogical Crystallography*, (Walter de Gruyter GmbH, 2016), 1–29, https://doi.org/10.1515/9783110417104-003.

35. C. Kasik, R. Pandey, A. Shah, and J. Sites, "Tellurium Oxide as a Back-Contact Buffer Layer for CdTe Solar Cells," in Conference Record of the IEEE Photovoltaic Specialists Conference, (2022). https://doi.org/10.1109/PVSC48317.2022.9938781.

36. Mayank Mate, "Arsenic Doping, Kinetic Behavior and Oxide Formation for Polycrystalline CdTe Thin Films Photovoltaics," (2024). [Online], https://hdl.handle.net/10217/235234.

37. Z. F. Lustig, "Improving Thin-Film Polycrystalline CdSeTe/CdTe Solar Cell Efficiencies Through Statistical Design of Experiments," (2022) [Online], https://hdl.handle.net/10217/235234.

38. V. Kumar, E. Artegiani, P. Punathil, et al., "Analysis of Se Co-Evaporation and Post-Selenization for Sb2Se3-Based Solar Cells," *ACS Applied Energy Materials* 4, no. 11 (2021): 12479–12486, https://doi.org/10.1021/acsaem.1c02301.